High-Speed Target Tracking Method for Compact HF Radar

Gan Liu, Yingwei Tian, *Member, IEEE*, Jing Yang, *Member, IEEE*, Shengbo Ma, and Biyang Wen

***Abstract*—Compact high-frequency (HF) surface wave radar can be used for remote sensing of sea surface dynamic parameters, such as winds, waves, and currents, as well as hard targets, such as ships and low-altitude aircrafts. Due to its small antenna aperture, compact HF radar usually has a large error in direction of arrival (DOA) estimation, which significantly reduces its accuracy of target tracking. For a high-speed target, the DOA estimation error is greater due to range migration and Doppler frequency migration as well as rapid change in the DOA of target echo. A high-speed target tracking method for compact HF radar is proposed in this article, which utilizes the zero-mean property of the DOA error. First, the generalized Radon Fourier transform is used to estimate the target's motion parameters, and the multiple signal classification algorithm is used to estimate the target's DOA. The original target track is obtained by combining the range and DOA estimates. Next, multiple positions on the original track are selected as the base points, and for each base point, a predicted track can be calculated based on the target motion parameter estimates, thus multiple predicted tracks are obtained. Then, these predicted tracks are screened according to their headings. The remaining predicted tracks after screening are fused to obtain the final track. Numerical simulations and field experiments demonstrate that this method reduces the impact of DOA error on tracking accuracy and expands the application of compact HF radar for high-speed target tracking.**

***Index Terms*—Compact high-frequency (HF) radar, direction of arrival (DOA), Doppler frequency migration (DFM), generalized Radon Fourier transform (GRFT), high-speed target tracking, range migration (RM).**

I. Introduction

HIGH-FREQUENCY (HF) radars have garnered significant attention due to their capabilities for over-the-horizon, near real-time and all-weather remote sensing of the sea surface [1]. Among them, compact HF surface wave radar has been widely deployed in coastal areas due to its small installation footprint, ease of maintenance, low power consumption, and low cost [2]. In recent years, compact HF radar has made great progress in the measurement of sea surface dynamic parameters, such as winds, waves, and currents [3], [4], [5], as well as in the detection and tracking of low-speed targets, such as ships navigating on the sea surface [6], [7], [8], but little has been reported about its tracking of high-speed targets such as low-flying aircrafts, missiles and speedboats.

In general, target tracking for compact HF radar follows these steps [9], [10]. First, the target is detected from the range-Doppler (RD) map using the constant false alarm rate (CFAR) detection [11] and its range and radial velocity are estimated. Then, the digital beam forming or direction finding (DF) algorithm, such as multiple signal classification (MUSIC) is used to estimate the direction of arrival (DOA) of the target [12], [13]. By combining range and DOA estimates, the target track is obtained. Compact HF radars, which utilize crossed-loop/monopole (CLM) antennas [14] or small aperture antenna arrays [15], offer greater flexibility in installation and maintenance than phased array radars with large aperture antennas [16]. However, this flexibility comes at the expense of spatial gain and resolution, and the reduced accuracy in DOA estimation leads to increased track deviation.

For high-speed target tracking, the DOA error and its effect on tracking accuracy is more serious. In order to obtain a sufficiently high signal-to-noise ratio (SNR), HF radars generally use a long coherent integration time (CIT) for hard target detection. High-speed targets usually undergo large changes in range and radial velocity during a long CIT, which results in the expansion of target echoes in the range dimension and the Doppler frequency dimension in the RD spectrum, two phenomena commonly referred to as range migration (RM) and Doppler frequency migration (DFM) [17], [18], [19]. On the one hand, RM and DFM make it difficult to detect the target and estimate its range and radial velocity from RD spectrum. On the other hand, RM and DFM increase the DOA estimation error of compact HF radars that typically use DF algorithms, since they reduce the SNR of echoes used for DOA estimation. In addition, the long CIT also makes the target's DOA likely to change drastically, which significantly limits the number of snapshots used for DOA estimation and thus increases the error. Reducing the CIT may solve these problems [16], but it also reduces the SNR and worsens the target detection performance.

Significant efforts have been devoted to enhancing the accuracy of DOA estimation. The time–frequency-MUSIC algorithm effectively mitigates nonstationarity caused by Doppler frequency variations and improves the azimuth estimation

Manuscript received 5 May 2024; revised 8 June 2024 and 23 June 2024; accepted 15 July 2024. Date of publication 22 July 2024; date of current version 5 August 2024. This work was supported in part by the National Key R&D Program of China under Grant 2022YFC2806300, in part by the National Natural Science Foundation of China under Grant 62071337, in part by the Natural Science Foundation of Hubei Province under Grant 2022CFB055, and in part by the Guangdong Basic and Applied Basic Research Foundation under Grant 2024A1515011961. *(Corresponding authors: Yingwei Tian; Jing Yang.)*

Gan Liu, Jing Yang, Shengbo Ma, and Biyang Wen are with the School of Electronic Information, Wuhan University, Wuhan 430072, China (e-mail: liugan@whu.edu.cn; janeyang628@whu.edu.cn; mashengbo@whu.edu.cn; bywen@whu.edu.cn).

Yingwei Tian is with the School of Electronic Information, Wuhan University, Wuhan 430072, China, and also with the Wuhan University Shenzhen Research Institute, Shenzhen 518057, China (e-mail: tianyw@whu.edu.cn).

Digital Object Identifier 10.1109/JSTARS.2024.3431535

accuracy of nonstationary targets [20]. In addition, a crossed-loop processing method ignores the amplitude information of monopole and calibrates the distortion of two loops, leading to improved DOA estimation accuracy of CLM antenna-based HF radar [21]. For coherent DOA estimation in sea surface observation, a method involving covariance matrix reconstruction and subspace estimation has been proposed [22]. Furthermore, to achieve a narrower beamwidth, a compact array combining two CLM antennas has been proposed [23]. These methods can improve the DOA estimation accuracy of compact HF radars to some extent, but for high-speed target tracking, these methods either cannot be used directly or have limited effectiveness.

Another class of methods directly optimizes the target track to enhance tracking accuracy. Some of the commonly used ones include Kalman filter [24], [25], particle filter [26], α-β filter [27], nearest neighbor data association [28], multiple hypothesis tracking [29], joint probabilistic data association [30], etc. In the case of large DOA errors, these methods are usually not satisfactory, and may even deteriorate the accuracy of target tracking. Sun et al. [7] employed Doppler velocity, azimuth trend, and course accumulated from consecutive observations to jointly re-estimate the azimuth and course of slow-speed maritime targets, thereby enhancing output track accuracy, but the case of high-speed target tracking was excluded. Artificial intelligence-based tracking methods [31], [32] have shown advantages in tracking accuracy, but they demand a substantial volume of data for network training and the transfer learning capabilities of the trained network are usually limited. In addition, joint tracking with multiple HF radars can improve tracking accuracy but requires costly hardware support [33], [34], [8].

In summary, so far there is no applicable method for compact HF radar high-speed target tracking. In order to solve the difficulties in target detection and parameter estimation caused by RM and DFM, generalized Radon Fourier transform (GRFT) [35], a method based on parameter searching, is used in this article, which can simultaneously achieve target detection and estimation of motion parameters such as range and speed. In addition, although the DOA estimation error of compact HF radar is large, especially when the target speed is high, it generally conforms to a zero-mean Gaussian distribution. This property is utilized in this article to propose a target tracking method for compact HF radar that can weaken the effect of DOA estimation error on tracking accuracy.

The proposed method is mainly divided into four steps. First, the GRFT is used to estimate the target's motion parameters, such as range and speed. The MUSIC algorithm is used to estimate the DOA of target echo. By combining the range and DOA information, the original target track is obtained. Second, the target's motion parameter estimates are used to calculate multiple predicted target tracks on the basis of the original track. Third, the predicted tracks are screened according to their average headings to remove those that are significantly different from the majority. Fourth, the remaining predicted tracks after screening are fused to obtain the final track.

The rest of this article is organized as follows. Section II outlines the problems in high-speed target tracking with compact HF radar. Section III details the steps of the proposed method.

TABLE I
COMPACT HF RADAR PARAMETERS

Parameter	Symbol	Value
Carrier frequency	f_c	13 MHz
Sweep bandwidth	B	300 kHz
PRI	T_r	0.27 s
Pulse number in a CPI	M	256
CPI	MT_r	69.12 s
Range resolution	ΔR	500 m
Radial velocity resolution	ΔV_r	0.167 m/s
Maximum detection range	–	64 km

In Section IV, the effectiveness of the proposed method is validated through numerical simulations. Section V further verifies the proposed method using field experimental data. Finally, Section VI concludes this article.

II. Problem Formulation

In this article, high-speed targets refer to those that induce significant RM and DFM during a coherent processing interval (CPI), e.g., low-flying aircrafts, missiles, and speedboats, and low-speed targets are those with negligible RM and DFM, e.g., slow ships navigating on the sea surface. Taking the radar used in the experimental part of this article as an example, whose operating parameters are listed in Table I, if the target is assumed to have a constant velocity (CV) within a CPI, RM can be generated when the target's velocity exceeds 7.23 m/s, and if the target is assumed to have a constant acceleration (CA) within a CPI, DFM can be generated when the acceleration exceeds 0.0024 m/s^2.

A. RM and DFM

The transmitting signal of HF radar using linear frequency modulated continuous waveform is expressed as

$$s_T\left(\tilde{t}\right) = \mathrm{rect}\left(\frac{\tilde{t}}{T_p}\right)\exp\left(j2\pi f_c\tilde{t}\right)\exp\left(j\pi\mu\tilde{t}^2\right) \tag{1}$$

where $\tilde{t}$ is the fast time, $\mathrm{rect}(\cdot) = \begin{cases}1, & |\cdot| \leqslant 1/2\\ 0, & |\cdot| > 1/2\end{cases}$, T_p is the pulse duration, f_c is the carrier frequency, $\mu = B/T_p$ is the chirp rate, and B is the sweep bandwidth.

Then, the backscattering echo of a target is

$$s_R\left(\tilde{t}\right) = \sigma_r\,\mathrm{rect}\left(\frac{\tilde{t}-t_d}{T_p}\right)\exp\left[j2\pi f_c(\tilde{t}-t_d)\right] \times\exp\left[j\pi\mu\left(\tilde{t}-t_d\right)^2\right] \tag{2}$$

where σ_r is the target reflectivity and t_d is the time delay.

Pulse compression of the echo yields the following 2-D signal, which can also be called the range–time (RT) spectrum [17]:

$$s_C\left(t_m,\tilde{r}\right) = A_r\mathrm{sinc}\left[\frac{2B\left(\tilde{r}-r(t_m)\right)}{c}\right]\exp\left[-j\frac{4\pi r(t_m)}{\lambda}\right] \tag{3}$$

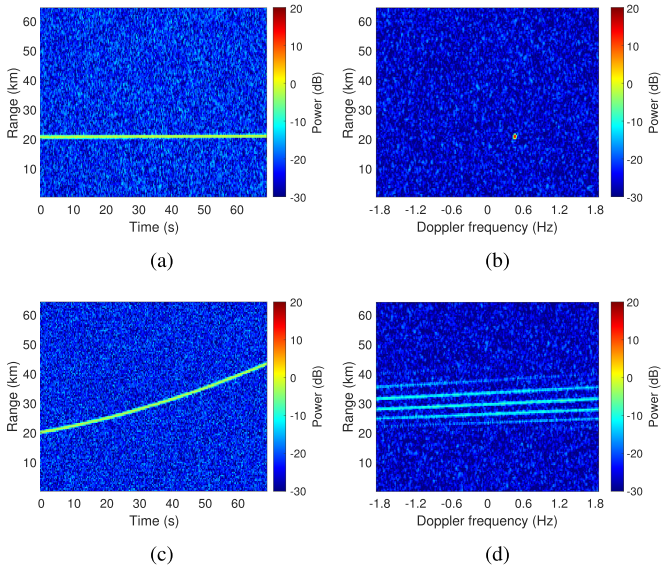

Fig. 1. (a) Simulated RT map for a low-speed target. (b) Simulated RD map for a low-speed target. (c) Simulated RT map for a high-speed target. (d) Simulated RD map for a high-speed target.

where $t_m = mT_r (m = 0, 1, \ldots, M-1)$ denotes the slow time, m is the pulse index, T_r is the pulse repetition interval (PRI), M is the number of pulses in a CPI, c is the speed of light, $\tilde{r} = c\tilde{t}/2$, A_r denotes the echo amplitude after pulse compression, $\mathrm{sinc}(\cdot)$ is the sinc function, $r(t_m)$ denotes the target's range at t_m, and $\lambda = c/f_c$ is the signal wavelength.

With t_m as the horizontal axis and $\tilde{r}$ as the vertical axis, the amplitude of s_C can be shown using the RT map. It can be seen from (3) that the peak position along axis $\tilde{r}$ corresponds to the target range $r(t_m)$. If the change in target range over time exceeds the radar's range resolution $c/(2B)$, a shift in peak position over time can be observed on the RT map, a phenomenon known as RM.

By Fourier transforming s_C along the t_m dimension, the RD spectrum is obtained, and its amplitude can be shown by an RD map. It can be derived from (3) that the peak position of the range bin where the target is located along the Doppler dimension corresponds to the target's radial velocity $\mathrm{d}r(t_m)/\mathrm{d}t$. If the radial velocity varies within a CPI beyond the velocity resolution $\lambda/(2MT_r)$, a Doppler-dimensional expansion of the target echo is seen on the RD map, a phenomenon known as DFM.

Fig. 1(a) and 1(c) shows the simulated RT maps of HF radar for a low-speed and a high-speed target moving away from the radar, respectively. The range of the horizontal axes corresponds to the CPI which is 69.12 s. The initial radial velocity of the low-speed target is 5 m/s, and its radial acceleration is 0.002 m/s^2. The initial radial velocity and radial acceleration of the high-speed target are 200 m/s and 2 m/s^2, respectively. To facilitate observation, the echo amplitudes of the two targets are set to be the same and do not vary with range. The radar's range resolution and velocity resolution are 0.5 km and 0.167 m/s, respectively. The low-speed target's range varies less than the range resolution within a CPI, so its path looks like a horizontal straight line. The range variation of the high-speed target exceeds the range resolution, resulting in RM, which is reflected on the RT map as a curved path spanning multiple range bins.

Fig. 1(b) and 1(d) illustrates the RD maps of low-speed target and high-speed target, respectively. The echo of low-speed target converge at a point with an SNR much higher than that on the RT map, which is favorable for target detection and parameter estimation. In contrast, due to the presence of RM and DFM, the echo of high-speed target has a wide distribution on the RD map with a SNR not increased relative to that on the RT map. This is not only detrimental to target detection, but also makes it difficult to estimate target motion parameters, such as range and radial velocity from RD map. In addition, the Doppler frequency of the high-speed target far exceeds the maximum unambiguous Doppler frequency of the radar, so the RD map suffers from Doppler ambiguity, i.e., the echo Doppler frequency shown on the RD map is not the true Doppler frequency. This problem makes it impossible to estimate the target radial speed from the RD map.

B. DOA Estimation

The high speed of target not only makes the detection and motion parameter estimation difficult, but also deteriorates the already poor DOA estimation accuracy of the compact HF radar. In order to improve the echo DOA resolution of small aperture array, compact HF radar usually uses the MUSIC algorithm, which decomposes the echo covariance matrix into signal and noise subspaces and utilizes the inherent orthogonality between them to achieve DOA estimation. In practice, the covariance matrix is generally estimated from a finite number of data snapshots as follows:

$$\hat{\mathbf{R}} = \frac{1}{N_s}\sum_{s=1}^{N_s} \mathbf{z_s}\mathbf{z_s}^H$$
$$\mathbf{z_s} = [z_{s1}, z_{s2}, \ldots, z_{sN_a}]^T \tag{4}$$

where $\hat{\mathbf{R}}$ is the covariance matrix, N_s is the number of snapshots, $\mathbf{z_s} \in \mathbf{C}^{N_a \times 1}$ denotes the sth snapshot, $[\cdot]^H$ is the conjugate transpose operation, N_a is the number of antenna array elements, $[\cdot]^T$ is the transpose operation, and z_{s1}, z_{s2},..., z_{sN_a} are the echoes received by different array elements.

It has been derived that the estimation error of MUSIC algorithm conforms to an asymptotically jointly Gaussian distribution with zero mean and variance given by [21], [36]

$$\mathrm{var}(\epsilon_\theta) = \frac{1}{2N_s \cdot \mathrm{SNR}}\left(1 + \frac{1}{2\mathrm{SNR}}\right) \tag{5}$$

where ϵ_θ denotes the DOA estimation error, and SNR is the SNR of target echo.

For the low-speed target, the echo of each array element $z_{sa}(a = 1, 2, \ldots, N_a)$ in the snapshot $\mathbf{z_s}$ is generally taken from the target-located RD bin of the RD spectrum of this array element, and its SNR is much higher than that of the RT spectrum due to coherent integration. For the high-speed target, due to the expansion of target echo in the RD spectrum caused by RM

and DFM, z_{sa} is taken from the target-located range bin of the RT spectrum. Therefore, the SNR of the echo used for DOA estimation for a high-speed target is much lower than that for a low-speed target, provided that the radar cross sections (RCSs) of the two targets are the same, which results in higher DOA estimation error according to (5).

In addition, the MUSIC algorithm requires that the DOAs at the corresponding moments of all snapshots used for estimation of the covariance matrix $\hat{\mathbf{R}}$ are almost the same. Low-speed targets generally have little change in DOA over a long period of time, so multiple snapshots at different moments can be used, while high-speed targets tend to change DOA rapidly, which greatly limits the number of snapshots N_s. From (5), it is clear that the reduction in N_s also increases the DOA estimation error.[1]

In summary, for high-speed target tracking with compact HF radars, it is important to address not only the effects of RM and DFM on target detection and motion parameter estimation, but also the effects of large DOA estimation errors on target localization.

III. Proposed Method

In order to solve the difficulties caused by RM and DFM in target detection and motion parameter estimation, the GRFT algorithm based on parameter searching is adopted. This algorithm not only realizes long-time coherent integration of high-speed target echoes, which enhances the SNR and thus improves the target detection, but also provides estimates of multiple motion parameters.

Although the DOA estimation error of compact HF radar is large, previous studies [36], [21] have proved that it always follows a zero-mean Gaussian distribution. Based on this property, a method is proposed to suppress the influence of DOA error on tracking accuracy by averaging multiple predicted tracks corresponding to different DOA estimates to realize mutual cancellation of DOA errors. The flow of the algorithm is shown in Fig. 2, which is divided into four main stages. Each stage is explained in detail as follows.

Fig. 3 shows the geometric relationship between the target and radar. Point O denotes the radar's location, and the arc from A to B is the target track. A circular motion model is used in this article, because general curvilinear motion can be decomposed into multiple small segments of circular motion, and the most common rectilinear motion can also be regarded as circular motion with zero curvature.

Note that in this article the term "track" refers to the projection of the true track on the 2-D horizontal plane. Since the compact HF radar mainly aims at sea surface observation, the electromagnetic waves emitted are surface waves, so the radar does not have the ability to measure the altitude of the target. Accordingly, in the following, all the position and motion parameters of the target refer to their projections on the horizontal plane.

[1]When N_s is small, robust covariance estimation methods can be applied, and relevant references include [37], [38], and [39].

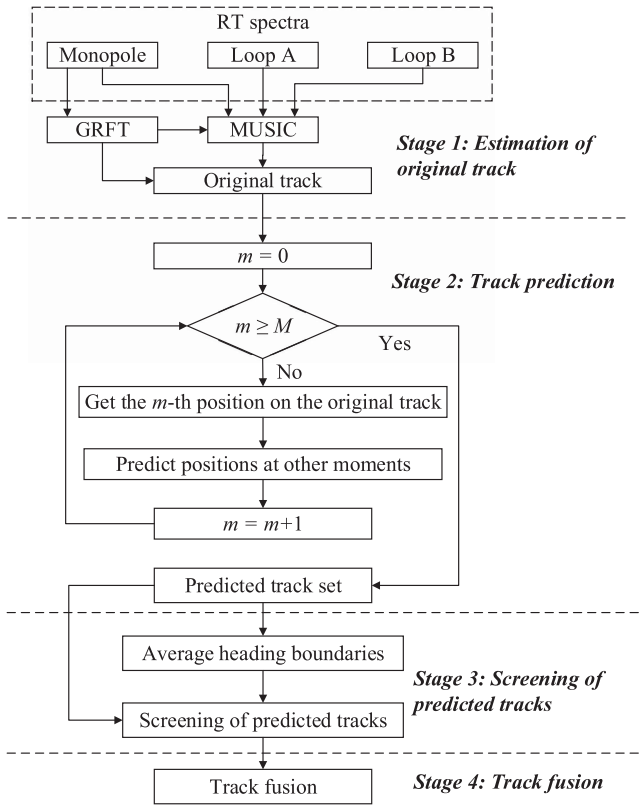

Fig. 2. Framework of the proposed method.

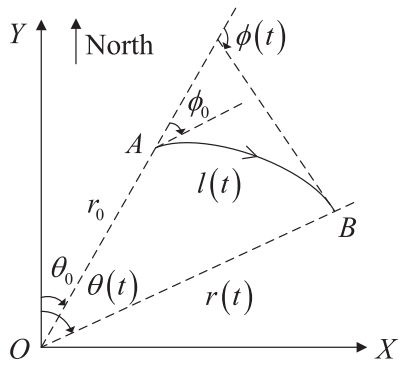

Fig. 3. Schematic diagram of target motion model. O: Radar's position, $A \rightarrow B$: the movement track of the target.

Suppose that the target speed can be expressed as

$$v(t) = v_0 + \sum_{d=1}^{\infty} \frac{a_d t^d}{d!} \tag{6}$$

where v_0 denotes the initial speed, and a_d is the initial value of the dth order derivative of the speed.

The length of the target's track is

$$l(t) = \int_0^t v(\tau)\mathrm{d}\tau. \tag{7}$$

Define the angle $\phi(t)$ that rotates clockwise from the initial radar radial direction $\overrightarrow{OA}$ to the target heading as the projection

angle, which is given by

$$\phi(t) = \phi_0 + \kappa l(t) \tag{8}$$

where ϕ_0 is the initial projection angle and κ is the curvature of circular motion. In this article, $\kappa > 0$ means the target moves in a clockwise direction, $\kappa < 0$ indicates a counterclockwise motion, and $\kappa = 0$ corresponds to a rectilinear motion.

The target's range $r(t)$ can be given as

$$r(t) = \sqrt{\left[r_0 + \int_0^t v(\tau)\cos\phi(\tau)\mathrm{d}\tau\right]^2 + \left[\int_0^t v(\tau)\sin\phi(\tau)\mathrm{d}\tau\right]^2} \tag{9}$$

where r_0 is the initial range.

The angle $\theta(t)$ that rotates clockwise from due north to the radar-to-target line is called the DOA, and its initial value is θ_0.

A. Estimation of Original Track

1) Estimation of Motion Parameters Based on GRFT: As shown in Fig. 2, in this article, the GRFT algorithm is used to estimate the target motion parameters from the RT spectrum corresponding to the monopole element of the CLM antenna, because the echo SNR of the monopole is usually the highest.

The discrete form expression for the GRFT of the RT spectrum is as follows [17], [18], [19]:

$$G_{\mathrm{GRFT}}(\Xi_s) = \sum_{m=0}^{M-1} s_C\left(t_m, r_s(t_m)\right)\exp\left[\mathrm{j}4\pi\frac{r_s(t_m)}{\lambda}\right] \tag{10}$$

where $\Xi_s = [r_{0\,s}, v_{0\,s}, a_{1\,s}, a_{2\,s}, \ldots, \phi_{0\,s}, \kappa_s]$ is a vector composed of all searching motion parameters, including searching initial range $r_{0\,s}$, searching initial speed $v_{0\,s}$, searching initial first-order derivative of speed $a_{1\,s}$, searching initial second-order derivative of speed $a_{2\,s}$ and searching initial higher-order derivatives, searching initial projection angle $\phi_{0\,s}$, and searching curvature κ_s. $r_s(t_m)$ is the target's range at t_m calculated by replacing the corresponding true parameters in (6)–(9) with the above-mentioned searching parameters. $s_C(t_m, r_s(t_m))$ is the value of the RT spectrum $s_C(t_m, \tilde{r})$ at $\tilde{r} = r_s(t_m)$.

In theory, the abstract value of GRFT output reaches its maximum value when all the searching parameters equal their corresponding true parameters. This can be proved by inserting (3) into (10), which yields

$$G_{\mathrm{GRFT}}(\Xi_s) = \sum_{m=0}^{M-1} A_r \mathrm{sinc}\left[\frac{2B\left(r_s(t_m) - r(t_m)\right)}{c}\right] \times \exp\left[j4\pi\frac{r_s(t_m) - r(t_m)}{\lambda}\right]. \tag{11}$$

Apparently $|G_{\mathrm{GRFT}}(\Xi_s)|$ is maximum when $r_s(t_m) = r(t_m)$ $(m = 0, 1, \ldots, M-1)$, which can be satisfied when $\Xi_s = \Xi$, where $\Xi = [r_0, v_0, a_1, a_2, \ldots, \phi_0, \kappa]$.

Based on the above-mentioned principle, GRFT-based target detection and motion parameter estimation are realized by the following steps.

1) Set the searching scopes for all motion parameters.
2) Iterate through all combinations of searching parameter values and compute the corresponding GRFT outputs according to (10).
3) Perform CFAR detection to confirm the presence of target and obtain the motion parameter estimates using the following equation:

$$\hat{\Xi} = \arg\max_{\Xi_s} |G_{\mathrm{GRFT}}(\Xi_s)|, \text{ s.t. } |G_{\mathrm{GRFT}}(\Xi_s)| \geq \gamma \tag{12}$$

where $\hat{\Xi} = [\hat{r}_0, \hat{v}_0, \hat{a}_1, \hat{a}_2, \ldots, \hat{\phi}_0, \hat{\kappa}]$ is the vector composed of parameter estimates, γ is the detection threshold determined by the desired false alarm probability [40].
4) By replacing the true parameters in (6)–(9) with their corresponding estimates in $\hat{\Xi}$, the target range estimate $\hat{r}(t_m)(m = 0, 1, \ldots, M-1)$ is calculated, which is also denoted by $\hat{r}_m$ for simplicity in the following text.

It should be noted that there is ambiguity in the estimation of initial projection angle and curvature, i.e., there should be two vectors of estimates obtained: $\hat{\Xi}$ and $\hat{\Xi}' = [\hat{r}_0, \hat{v}_0, \hat{a}_1, \hat{a}_2, \ldots, -\hat{\phi}_0, -\hat{\kappa}]$. It can be derived from (6)–(10) that the two vectors result in equal range estimate $\hat{r}_m$ and thus equal GRFT outputs. This ambiguity can be removed by restricting the searching scope of $\phi_{0\,s}$ or κ_s to positive or negative numbers.

2) DOA Estimation Based on MUSIC: As shown in Fig. 2, the MUSIC algorithm is used to estimate the target's DOA from the RT spectra of the three antenna elements integrated into a CLM antenna. Thus, N_a in (4) is set to 3.

Since the target's DOA changes rapidly due to the target's high speed, the DOA is estimated once for each pulse moment, and the number of snapshots N_s used in each estimation is set to 1.

For the pulse moment t_m, the echo of each antenna element $z_{1a}(a = 1, 2, 3)$ in the snapshot comes from the target-located range bin in the RT spectrum $s_C(t_m, \hat{r}_m)$ corresponding to this antenna element, where $\hat{r}_m$ is already obtained by GRFT. The DOA estimation result for each pulse moment is denoted as $\hat{\theta}_m$.

3) Synthesis of Original Track: By combining the target's DOA and range estimates, the original target track in Cartesian coordinates using the radar's position as the origin can be synthesized

$$\begin{aligned}\hat{\mathbf{U}} &= \{(\hat{x}_m, \hat{y}_m)\,|m = 0, 1, \ldots, M-1\} \\ \hat{x}_m &= \hat{r}_m \sin\hat{\theta}_m \\ \hat{y}_m &= \hat{r}_m \cos\hat{\theta}_m\end{aligned} \tag{13}$$

where $\hat{\mathbf{U}}$ is the original track, $\hat{x}_m$ and $\hat{y}_m$ are the x-axis and y-axis coordinates of the estimated target position at t_m, respectively.

B. Track Prediction

Fig. 4 depicts the schematic of track prediction within the Cartesian coordinate system. The specific steps are as follows.

Step 1, calculate the correlation coefficient between the DOA estimate series $\hat{\mathbf{\Theta}} = [\hat{\theta}_0, \hat{\theta}_1, \ldots, \hat{\theta}_{M-1}]$ and the slow time series

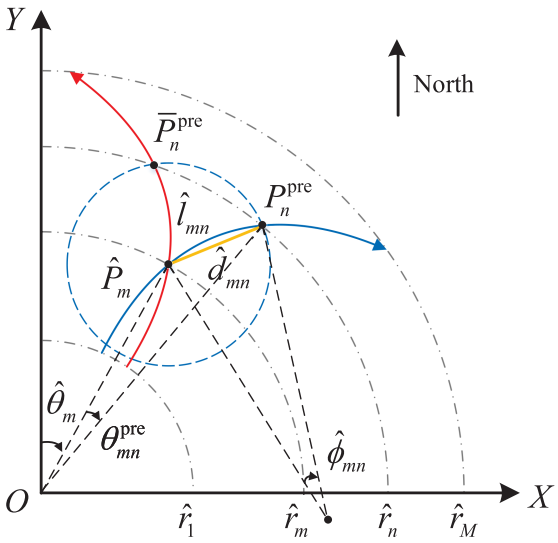

Fig. 4. Schematic diagram of calculating predicted target track.

$\mathbf{T} = [T_r, 2T_r, \ldots, MT_r]$ according to the following equation:

$$\rho = \frac{\mathrm{Cov}\left(\hat{\mathbf{\Theta}}, \mathbf{T}\right)}{D^{\frac{1}{2}}\left(\hat{\mathbf{\Theta}}\right) \cdot D^{\frac{1}{2}}\left(\mathbf{T}\right)} \tag{14}$$

where $D(\hat{\mathbf{\Theta}})$ and $D(\mathbf{T})$ denote the variance of $\hat{\mathbf{\Theta}}$ and $\mathbf{T}$, respectively, and $\mathrm{Cov}(\hat{\mathbf{\Theta}}, \mathbf{T})$ is the covariance between $\hat{\mathbf{\Theta}}$ and $\mathbf{T}$. $\rho > 0$ means that the change trend of $\hat{\theta}_m$ over time is mainly increasing, $\rho < 0$ indicates that the trend is decreasing, and $\rho = 0$ implies that $\hat{\theta}_m$ does not change over time, i.e., the target moves in the radial direction of the radar. It should be noted that the proposed method requires that the target's DOA maintains a trend over a CPI, either increasing, decreasing, or unchanged.

Step 2, the target position at $t_m (m = 0, 1, \ldots, M-1)$ on the original track is selected as the base point of the mth predicted track, which is denoted as $\hat{P}_m$ in Fig. 4. The distance $\hat{d}_{mn}$ between the target positions at t_n $(n = 0, 1, \ldots, M-1)$ and t_m can be calculated using the following equations:

$$\begin{aligned} \hat{d}_{mn} &= \left| \frac{2}{\hat{\kappa}} \sin \frac{\hat{\phi}_{mn}}{2} \right| \\ \hat{\phi}_{mn} &= \hat{\kappa} \hat{l}_{mn} \\ \hat{l}_{mn} &= \int_{mT_r}^{nT_r} \hat{v}(t) dt \end{aligned} \tag{15}$$

where $\hat{\phi}_{mn}$ is the estimated angle between the target's headings at t_m and t_n, $\hat{l}_{mn}$ is the estimated length of the circular track of the target between moments t_m and t_n, and $\hat{v}(t)$ is the target speed estimate, which is obtained by replacing v_0 and a_d in (6) with their corresponding estimates $\hat{v}_0$ and $\hat{a}_d$.

Step 3, draw a circle with $\hat{P}_m$ as the center and $\hat{d}_{mn}$ as the radius. Draw another circle with radar position O as the center and target range estimate $\hat{r}_n$ as the radius. The predicted target position at t_n should be on both of these two circles, so their intersection point can be regarded as the predicted position at t_n. However, as shown in Fig. 4, there may be two intersection points P_n^{pre} and $\overline{P}_n^{\text{pre}}$. Apparently the difference between the DOA of the predicted position at t_n and the DOA of $\hat{P}_m$ is

$$\theta_{mn}^{\text{pre}} = \arccos \left| \frac{\hat{r}_m^2 + \hat{r}_n^2 - \hat{d}_{mn}^2}{2\hat{r}_m \hat{r}_n} \right|. \tag{16}$$

Step 4, using the value of ρ, the DOA of the predicted position at t_n can be determined as

$$\theta_n^{\text{pre},m} = \begin{cases} \hat{\theta}_m + \theta_{mn}^{\text{pre}}, \ \rho\,(n-m) > 0 \\ \hat{\theta}_m - \theta_{mn}^{\text{pre}}, \ \rho\,(n-m) < 0 \\ \hat{\theta}_m, \ \rho\,(n-m) = 0. \end{cases} \tag{17}$$

As depicted in Fig. 4, when $n > m$, the target's position at t_n should be P_n^{pre} if $\rho > 0$, and $\overline{P}_n^{\text{pre}}$ if $\rho < 0$. For $\rho = 0$, i.e., the case that the target is moving in the radial direction of the radar, the target's DOA at t_n should be the same as at t_m.

Step 5, change the value of t_n and repeat steps 2–4 to calculate the predicted positions at all other moments. Combining these predicted positions gives the mth predicted track with $\hat{P}_m$ as the base point, which can be denoted as

$$\begin{aligned} \mathbf{U}^{\text{pre},m} &= \{(x_n^{\text{pre},m}, y_n^{\text{pre},m}) \,|n = 0, 1, \ldots, M-1\} \\ x_n^{\text{pre},m} &= \hat{r}_n \sin \theta_n^{\text{pre},m} \\ y_n^{\text{pre},m} &= \hat{r}_n \cos \theta_n^{\text{pre},m}. \end{aligned} \tag{18}$$

Step 6, change the value of m and repeat steps 2–5 to calculate predicted tracks with target positions at other moments on the original track as the base points, thereby composing a set of predicted tracks, which is expressed as

$$\mathbf{S}^{\text{pre}} = \{\mathbf{U}^{\text{pre},m} \,|m = 0, 1, \ldots, M-1\}. \tag{19}$$

C. Screening of Predicted Tracks

In Section III-B, multiple predicted tracks are obtained within a CPI. In order to reduce the tracking error, before fusing these tracks into a single one, it is beneficial to screen them and remove those that deviate too much from the actual track. The specific steps are as follows.

Step 1, calculate the average heading of each predicted track using the following equation:

$$\begin{aligned} \psi^{\text{pre},m} = \frac{1}{M-1} \sum_{n=0}^{M-2} \text{angle}[&y_{n+1}^{\text{pre},m} - y_n^{\text{pre},m} \\ &+ j(x_{n+1}^{\text{pre},m} - x_n^{\text{pre},m})] \end{aligned} \tag{20}$$

where $\psi^{\text{pre},m} \in (-\pi, \pi]$ is the angle between the due north and the target heading direction, and angle$(\cdot)$ is the function that returns the phase angle of a complex number.

Then, the set of average headings for all predicted tracks is obtained

$$\mathbf{\Psi}^{\text{pre}} = \{\psi^{\text{pre},m} \,|m = 0, 1, \ldots, M-1\}. \tag{21}$$

Step 2, set the upper boundary χ_{r} and lower boundary χ_{l} of average heading used to screen the predicted tracks.

If the histogram of average heading set is drawn and the center value of the bin containing the most elements is defined as $\psi_{\mathrm{c}}^{\mathrm{pre}}$, then χ_{l} and χ_{r} should satisfy the following equations:

$$\begin{cases} \frac{\chi_{\mathrm{l}}+\chi_{\mathrm{r}}}{2} = \psi_{\mathrm{c}}^{\mathrm{pre}} \\ \psi_{\min}^{\mathrm{pre}} \leqslant \chi_{\mathrm{l}} < \chi_{\mathrm{r}} \leqslant \psi_{\max}^{\mathrm{pre}} \\ \mathrm{num}\left\{m \,|\chi_{\mathrm{l}} \leqslant \psi^{\mathrm{pre},m} \leqslant \chi_{\mathrm{r}}\right\}/M \leqslant \xi \end{cases} \tag{22}$$

where $\psi_{\min}^{\mathrm{pre}}$ is the minimum value of $\mathbf{\Psi}^{\mathrm{pre}}$ and $\psi_{\max}^{\mathrm{pre}}$ is its maximum value, num$\{\cdot\}$ returns the number of elements that satisfy the specified condition, ξ is the retention proportion of predicted tracks.

Specifically, χ_{l} and χ_{r} are calculated according to the following steps.

1) Set the values of χ_{l}' and χ_{r}' according to the following equations:

$$\begin{cases} \chi_{\mathrm{l}}' = \psi_{\min}^{\mathrm{pre}}, \chi_{\mathrm{r}}' = \psi_{\max}^{\mathrm{pre}}, \text{ if } 2\psi_{\mathrm{c}}^{\mathrm{pre}} = \psi_{\min}^{\mathrm{pre}} + \psi_{\max}^{\mathrm{pre}} \\ \chi_{\mathrm{l}}' = \psi_{\min}^{\mathrm{pre}}, \chi_{\mathrm{r}}' = 2\psi_{\mathrm{c}}^{\mathrm{pre}} - \psi_{\min}^{\mathrm{pre}}, \text{ if } 2\psi_{\mathrm{c}}^{\mathrm{pre}} < \psi_{\min}^{\mathrm{pre}} \\ \quad + \psi_{\max}^{\mathrm{pre}} \\ \chi_{\mathrm{l}}' = 2\psi_{\mathrm{c}}^{\mathrm{pre}} - \psi_{\max}^{\mathrm{pre}}, \chi_{\mathrm{r}}' = \psi_{\max}^{\mathrm{pre}}, \text{ if } 2\psi_{\mathrm{c}}^{\mathrm{pre}} > \psi_{\min}^{\mathrm{pre}} \\ \quad + \psi_{\max}^{\mathrm{pre}}. \end{cases} \tag{23}$$

2) Calculate the number of average headings located in $[\chi_{\mathrm{l}}', \chi_{\mathrm{r}}']$, i.e., the value of num$\{m|\chi_{\mathrm{l}}' \leqslant \psi^{\mathrm{pre},m} \leqslant \chi_{\mathrm{r}}'\}$.

3) If num$\{m|\chi_{\mathrm{l}}' \leqslant \psi^{\mathrm{pre},m} \leqslant \chi_{\mathrm{r}}'\}/M \leqslant \xi$, then $\chi_{\mathrm{l}} = \chi_{\mathrm{l}}'$, $\chi_{\mathrm{r}} = \chi_{\mathrm{r}}'$. Otherwise, update χ_{l}' and χ_{r}' according to the following equations and repeat steps 2) and 3):

$$\chi_{\mathrm{l}}' = \chi_{\mathrm{l}}' + \chi_s,\ \chi_{\mathrm{r}}' = \chi_{\mathrm{r}}' - \chi_s \tag{24}$$

where χ_s is the step for updating χ_{l}' and χ_{r}', which can be set equal to the bin width of the histogram of the average heading set.

Step 3, the set of predicted tracks is screened with boundaries χ_{l} and χ_{r} to obtain the screened track set $\mathbf{S}^{\mathrm{scr}}$

$$\mathbf{S}^{\mathrm{scr}} = \left\{\mathbf{U}^{\mathrm{pre},m} \,|\chi_{\mathrm{l}} \leqslant \boldsymbol{\psi}^{\mathrm{pre},m} \leqslant \chi_{\mathrm{r}}\right\}. \tag{25}$$

D. Track Fusion

By performing averaging fusion on the remaining predicted tracks after screening, the final result of target tracking, i.e., the fusion track, is obtained

$$\begin{aligned} \mathbf{U}^{\mathrm{fus}} &= \frac{1}{I}\sum_{i=0}^{I-1}\mathbf{U}^{\mathrm{scr},i} \\ &= \left\{\left(\frac{1}{I}\sum_{i=0}^{I-1}x_n^{\mathrm{scr},i}, \frac{1}{I}\sum_{i=0}^{I-1}y_n^{\mathrm{scr},i}\right)|n=0,1,\ldots,M-1\right\} \end{aligned} \tag{26}$$

where $I \leqslant M\xi$ is the number of tracks in $\mathbf{S}^{\mathrm{scr}}$, $\mathbf{U}^{\mathrm{scr},i}$ denotes the ith track in $\mathbf{S}^{\mathrm{scr}}$, $x_n^{\mathrm{scr},i}$ and $y_n^{\mathrm{scr},i}$ are the coordinates of the target position at t_n on the ith track.

Since the track fusion in this article is limited to one CPI, the fragmentation of tracks involved in the fusion is not considered. If fusion is performed for longer tracks, fragmentation is likely to occur due to SNR fluctuation of target echoes, or interference from sea clutter, etc., thus a reasonable track association and fusion algorithm is required [41], [42].

Algorithm 1: High-Speed Target Tracking Method.

Input: RT spectra corresponding to three receiving antenna elements of compact HF radar.

Output: Fusion track $\mathbf{U}^{\mathrm{fus}}$.

1: The GRFT algorithm is used to detect the target from the RT spectrum $s_C(t_m, \tilde{r})$ of the monopole antenna and to estimate the motion parameters according to (12). These estimates are then substituted into (6)–(9) to calculate the target range estimate of each pulse $\hat{r}_m$.

2: For the m-th pulse, the MUSIC algorithm is applied to the values of RT spectra of the three antenna elements at a range of $\hat{r}_m$ to obtain the target's DOA estimate $\hat{\theta}_m$. Follow this method to obtain the DOA estimates for other pulses.

3: According to (13), the original target track $\hat{\mathbf{U}}$ is obtained using the target's range and DOA estimates.

4: Calculate the correlation coefficient ρ between the DOA estimate series $\hat{\mathbf{\Theta}}$ and the slow time series $\mathbf{T}$ according to (14).

5: Follow the process below to calculate the set of predicted tracks $\mathbf{S}^{\mathrm{pre}}$.

for $m \leftarrow 0 : M-1$ **do**

Select the target position at t_m on the original track as the base point and get its DOA value $\hat{\theta}_m$.

for $n \leftarrow 0 : M-1$ **do**

Calculate the distance $\hat{d}_{mn}$ between the target positions at t_m and t_n according to (15).

Calculate the predicted DOA shift from m-th to n-th pulse $\theta_{mn}^{\mathrm{pre}}$ according to (16).

Calculate the predicted target's DOA $\theta_n^{\mathrm{pre},m}$ at t_n according to (17).

end for

The predicted target track $\mathbf{U}^{\mathrm{pre},m}$ with the target position at t_m on the original track as the base point is obtained according to (18).

end for

The set of predicted tracks $\mathbf{S}^{\mathrm{pre}}$ is obtained according to (19).

6: Follow the steps below to screen the predicted tracks.

6.a: Calculate the set of average headings of all predicted tracks $\mathbf{\Psi}^{\mathrm{pre}}$ according to (21).

6.b: Calculate the upper boundary χ_r and lower boundary χ_l of average heading according to (22).

6.c: Screen the set of predicted tracks $\mathbf{S}^{\mathrm{pre}}$ with χ_r and χ_l according to (25) to obtain the screened track set $\mathbf{S}^{\mathrm{scr}}$.

7: The tracks in $\mathbf{S}^{\mathrm{scr}}$ are fused according to (26) to obtain the fusion track $\mathbf{U}^{\mathrm{fus}}$.

The proposed method is summarized in Algorithm 1.

IV. Numerical Simulation

In this section, numerical simulations are performed to verify the algorithm proposed in this article.

TABLE II
TARGET PARAMETERS IN SIMULATION

Parameter	Symbol	Value
Initial range	r_0	20 km
Initial projection angle	ϕ_0	1 rad
Initial speed	v_0	200 m/s
Initial DOA	θ_0	–10°
Curvature	κ	5×10^{-5}* 0**

* This value is used in Section IV-B.
** This value is used in Section IV-C.

TABLE III
PARAMETER SEARCHING SCOPE OF GRFT

Searching parameter	Symbol	Scope
Initial range	r_{0s}	1.5: 0.05: 64 km
Initial speed	v_{0s}	0: 0.723: 300 m/s
Initial projection angle	ϕ_{0s}	$-\pi$: 0.0024: π rad
Curvature	κ_s	0: 1.5×10^{-7}: 1.5×10^{-4} rad/m

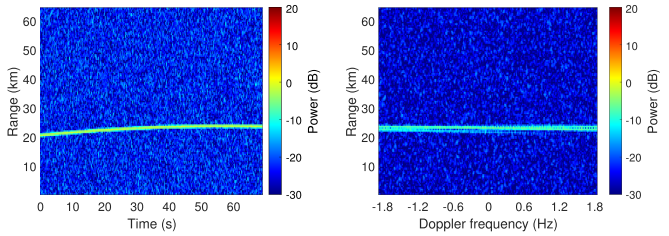

Fig. 5. Simulated echo spectra of a target in circular motion within a CPI. (a) RT map. (b) RD map.

A. Parameter Setting

In the numerical simulation, the radar parameters are set in accordance with the operating parameters of the compact HF radar used in the field experiment, which are detailed in Table I.

In addition, unless otherwise specified, the target parameters for simulation are set according to Table II. In order to reduce the computational complexity of GRFT, the simulation assumes a constant target speed and neglects its derivatives $a_d(d = 1, 2, \ldots)$.

According to the radar equation [43], for HF radar, the SNR of the target echo after pulse compression can be expressed as [44]

$$\mathrm{SNR} = \frac{4P_tG_tG_rL_s\lambda^2\Delta R\Delta\theta\Upsilon T_p}{(4\pi)^3 r k_B T_0 F (cT_r)^2} \tag{27}$$

where the meanings of some parameters and their values in this article are listed as follows.

1) P_t: radar transmission power, 200 W.
2) G_t: transmitting antenna gain, 1.
3) G_r: receiving antenna gain, 1.
4) L_s: system loss, 0.01.
5) λ: signal wavelength, 23.08 m.
6) $\Delta\theta$: radar azimuth resolution, 0.087 rad.
7) Υ: RCS, 0.1∼100 m^2.
8) T_p: pulse duration, 0.256 s.
9) r: target range, 1.5∼64 km.
10) k_B: Boltzmann constant, 1.38×10^{-23}J/K.
11) T_0: system Kelvin temperature, 290 K.
12) F: noise coefficient, 10^4.

The above-mentioned RCS scope is mainly for civil aircrafts [45], [46], as they are the observation objects of the field experiment in this article. Based on the above-mentioned equation, the echo SNR is calculated to be $-38\sim8$ dB. In order to check the performance of the proposed method at low SNR, the SNR is set to -38 dB in the following simulation unless otherwise specified.

Based on observations from previous field experiments, the DOA measurement error ϵ_θ of HF radar usually conforms to a Gaussian distribution with zero mean [21], i.e., $\epsilon_\theta \sim N(0, \sigma_\theta^2)$, where the standard deviation $\sigma_\theta \in [0, 25°]$. In the following simulation, unless otherwise specified, σ_θ is set to 25°.

Table III gives the parameter searching scopes of GRFT in this article. The lower and upper searching limits of initial range are determined by the blind range and maximum detection range of the compact HF radar, respectively. The upper searching limit of initial speed is set based on the maximum speed of the target of interest, i.e., civil aircrafts. It is deduced from (6)–(10) that the GRFT outputs corresponding to $(-\phi_{0s}, -\kappa_s)$ and (ϕ_{0s}, κ_s) are the same, holding other parameters constant, so the curvature searching scope is limited to nonnegative values.

As described in Section III-B, the proposed method of this article only addresses the case that the target's DOA maintains an increasing, or decreasing, or unchanged trend over a CPI. Thus, the change of the projection angle $\phi(t)$ within a CPI must be no greater than π, i.e.,

$$\kappa \int_0^{MT_r} v(\tau)\mathrm{d}\tau \leqslant \pi. \tag{28}$$

According to the above-mentioned formula, the maximum value of κ is calculated, which is taken as the upper limit of the searching curvature κ_s. The lower limit of κ_s corresponds to rectilinear motion.

The searching interval for each parameter is set based on the principle that if this parameter is varied at this interval, the resulting position shift of the target track does not exceed $\Delta R/10$, while other parameters remain unchanged.

B. Circular Motion

Fig. 5(a) and 5(b), respectively, shows the echo RT map and RD map of a target in circular motion simulated according to the parameters in Tables I and II. It should be noted that in order to see the target echo clearly, the echo intensities are increased equally when drawing these two maps. Obviously, both the RM and DFM are present, so RD map has no improvement in SNR relative to RT map, and it is difficult to estimate the target motion parameters directly from RD map.

Fig. 6(a) shows the original track within a CPI. As stated in Section III-A, the original track refers to the track synthesized using the range estimates from the GRFT algorithm and the

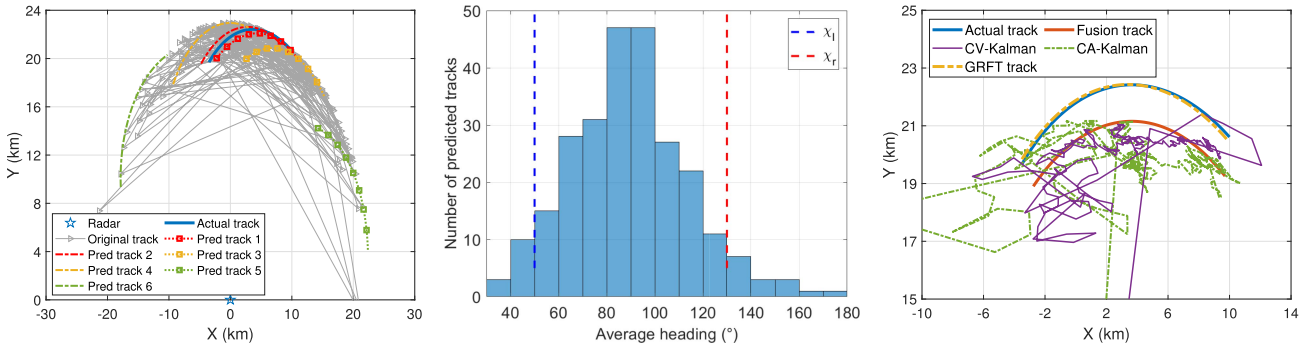

Fig. 6. Processing results of a simulated circular motion. (a) Original track and six predicted tracks. (b) Histogram of the average headings of all predicted tracks. (c) GRFT track, fusion track and results of CV-Kalman filter and CA-Kalman filter.

DOA estimates from the MUSIC algorithm. However, for the numerical simulations in Section IV, the DOA values used to synthesize the original track are the sums of the true DOA values and Gaussian random numbers with mean zero. The true DOA values refer to the DOA values of the actual track. The reason for doing this is to facilitate the simulation of various DOA estimation errors and thus testing the performance of the proposed method under different DOA errors. For the original track in Fig. 6(a), the standard deviation of the Gaussian random numbers is set to 25°. Due to this large standard deviation, the original track looks very confusing and far from a regular airplane track.

Fig. 6(a) also gives the actual track for comparison, i.e., the track synthesized using the real range and DOA values which are calculated based on the target parameters in Table II. It can be seen that the original track deviates significantly from the actual track, and the RMSE of its target localization is calculated to be 9.41 km.

The error in the original track comes partly from the DOA estimation error and partly from the range estimation error. To confirm that the former is much larger than the latter, the concept of GRFT track is defined, which refers to the track synthesized using the range estimates from the GRFT algorithm and the true DOAs. The GRFT track does not contain DOA error, but only range estimation error from the GRFT algorithm. It should be noted that the GRFT track is not available in practical target tracking because the true DOA values are unknown, and it is only used in this article to evaluate the range estimation error from the GRFT algorithm. In order to clearly observe the difference between the GRFT track and the actual track, they are both plotted in Fig. 6(b) with reduced axis ranges relative to Fig. 6(a). The GRFT track is highly consistent with the actual track, with an RMSE of 0.10 km. By comparing the GRFT track with the original track in Fig. 6(a), it can be determined that the large deviation of the original track relative to the actual track is mainly caused by the DOA error rather than GRFT estimation error.

Fig. 6(a) also demonstrates the predicted target tracks. Due to the large number of predicted tracks within a CPI, only six are drawn for ease of observation, and the DOA errors of their base points are respectively 3.77°, −3.60°, 17.50°, −17.44°, 55.07°, −52.28°. As can be seen, the predicted tracks are much smoother than the original track, and their trends of circular motion are obvious. The two predicted tracks of the same color (tracks 1 and 2, tracks 3 and 4, tracks 5 and 6) correspond to two base points with DOA errors of opposite signs and almost equal absolute values, so they are approximately symmetric with respect to the actual track in terms of DOA.

Fig. 6 shows a histogram of the average headings of all predicted tracks. According to the setting of the retention proportion $\xi = 0.8$, the lower boundary $\chi_l = 50°$ and the upper boundary $\chi_r = 130°$ for screening of predicted tracks are obtained.

Fig. 6(b) gives the processing result of the proposed method, i.e., the fusion track. For a clear view, the axis ranges are reduced relative to Fig. 6(a). For comparison, the processing results of two widely used tracking algorithms are also given, including the CV-Kalman filter and the CA-Kalman filter. Among these three tracks, the fusion track is the closest to the actual track. The processing results of CV-Kalman filter and CA-Kalman filter are messy and do not show the trend of circular movement at all. It should be noted that the fusion track seems to deviate significantly from the actual track compared to the GRFT track. However, the GRFT track is not available in real target tracking, because its DOA values are the true target DOA values which are unknown in practical applications. Therefore, the GRFT track cannot be used as the processing result of the proposed method, only the fusion track can.

The target localization RMSEs of the fusion track, CV-Kalman filter, CA-Kalman filter are 1.32, 3.46, and 11.61 km, respectively. Compared to the RMSE of the original track (9.41 km), CA-Kalman filter even worsens the accuracy of target localization. On the one hand, the RMSE of the fusion track (1.32 km) is much smaller than that of the original track (9.41 km), indicating that the DOA error contained in the original track has been significantly suppressed. On the other hand, the RMSE of the fusion track (1.32 km) is larger than that of the GRFT track (0.10 km), suggesting that the DOA error has not been completely eliminated.

C. Rectilinear Motion

Rectilinear motion can be regarded as circular motion with zero curvature. Fig. 7 shows the echo RT map and RD map

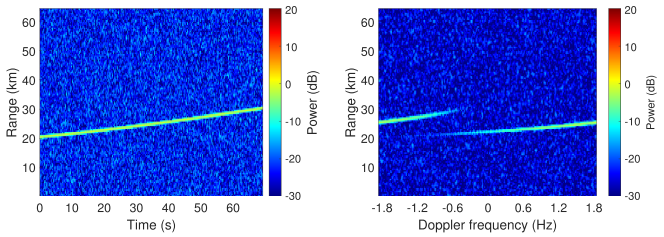

(a) (b)

Fig. 7. Simulated echo spectra of a target in rectilinear motion within a CPI. (a) RT map. (b) RD map.

simulated according to the parameters listed in Table II. It is clear that the echo spans multiple range bins and Doppler frequency bins, so the RM and DFM are present.

Fig. 8 shows the results of a simulation experiment. In Fig. 8(c), the GRFT track almost coincides with the actual track, and the RMSE of its target localization is 0.11 km, indicating that the parameter estimation errors of GRFT algorithm are small. However, in Fig. 8(a), the original track deviates greatly from the actual track, with an RMSE of 10.13 km. By comparing the original track and the GRFT track, it can be determined that the error in the original track is caused mainly by the large errors of the DOA values ($\sigma_\theta = 25^\circ$).

Fig. 8(a) also demonstrates six predicted tracks, which are all nearly straight lines. The DOA errors of their base points are 40.99°, -39.63°, 19.47°, -19.49°, 9.45° and -9.48°, respectively. The two tracks of the same color (tracks 1 and 2, tracks 3 and 4, tracks 5 and 6) correspond to two base points with DOA errors almost symmetric with respect to 0, so the two tracks are almost symmetric with respect to the actual track in terms of DOA.

Fig. 8(b) shows a histogram of the average headings of all predicted tracks within a CPI. The lower boundary of track screening is set to $\chi_1 = 30^\circ$ and the upper boundary is $\chi_r = 80^\circ$.

Fig. 8(c) shows the processing results of the proposed method, CV-Kalman filter and CA-Kalman filter, whose target localization RMSEs are 1.01, 4.77, and 10.73 km, respectively. The proposed method still shows the best tracking performance, whose result is the only one that approximates a straight line in form.

D. Monte Carlo Simulation

Figs. 6 and 8 just show the results of a single simulation experiment. Next, multiple Monte Carlo experiments are conducted to evaluate the performance of the proposed method more accurately. It should be noted that only the simulation results of circular motion are given below, since the simulation results of rectilinear motion are similar.

Fig. 9 shows the RMSEs of target motion parameter estimation using GRFT for different echo SNRs. The raw RMSEs are calculated with an SNR interval of 1 dB, and for each SNR 50 Monte Carlo experiments are performed. The red dashed line in each subgraph is the result of fitting the discrete raw RMSEs. It can be seen that for each motion parameter, the RMSE basically decreases with the increase of SNR. The processing results in Fig. 6 correspond to the case when SNR is minimum. Obviously, if the SNR is higher, the proposed method should perform better.

Fig. 10 shows the track localization errors for different GRFT searching intervals. The horizontal axis represents multiples of the original searching intervals, i.e., the intervals listed in Table III. For each multiple, 50 Monte Carlo experiments are performed.

When the multiple is less than 4, the RMSE of the GRFT track increases significantly with the increase of the multiple, but the RMSE of the original track hardly increases, which indicates that it is the DOA error rather than the GRFT estimation error that plays a major role in the original track error. When the multiple exceeds 4, the RMSEs of both the GRFT track and the original track increase with the multiple, and the difference between them gradually decreases, indicating that the GRFT estimation error has an increasing effect on the original track error.

Compared with the original track, the influence of DOA error in fusion track is suppressed, but the effect of GRFT estimation error cannot be reduced. So when the multiple is less than 4, the RMSE of the fusion track is much smaller than that of the original track, while when the multiple exceeds 4, the gap between them gradually decreases. Therefore, it is recommended that the searching intervals are smaller than four times the original searching intervals.

Fig. 11 shows the track RMSEs for different standard deviations of DOA error. Each RMSE value is the average of 50 Monte Carlo experiments. The RMSEs at $\sigma_\theta = 25^\circ$ are almost the same as those of the single experiment in Fig. 6, which proves the reliability of the latter. The RMSEs of all these four tracks increase with the increase of σ_θ, indicating that they are all affected by DOA errors. The RMSE of fusion track is the smallest, followed by the RMSE of CV-Kalman filter, and the RMSE of CA-Kalman filter is even larger than that of the original track. Obviously the proposed method is the most effective in suppressing the influence of DOA error on the original track, and the greater the DOA error, the more prominent the advantage of the proposed method.

In the previous simulations, the retention proportion ξ when screening the predicted tracks is set to 0.8. Fig. 12 shows the fusion track RMSEs for different ξ. Each RMSE value is the average of 50 Monte Carlo experiments. When σ_θ is less than 10°, the RMSE of fusion track decreases with the increase of ξ, indicating that when the DOA estimation error is small, the more predicted tracks involved in fusion, the smaller the error of fusion track. When σ_θ is greater than 15°, the RMSE first decreases and then increases with the increase of ξ, which indicates that when DOA estimation error is large, those predicted tracks with big errors must be removed before track fusion. Based on the simulation results, $\xi = 0.8$ is identified as the optimal value in this article.

V. Field Experiment

A. Experiment Background

On 3 April 2022, a field experiment was conducted in Wuhan, Hubei Province, China. The experiment lasted for 6 h. During the

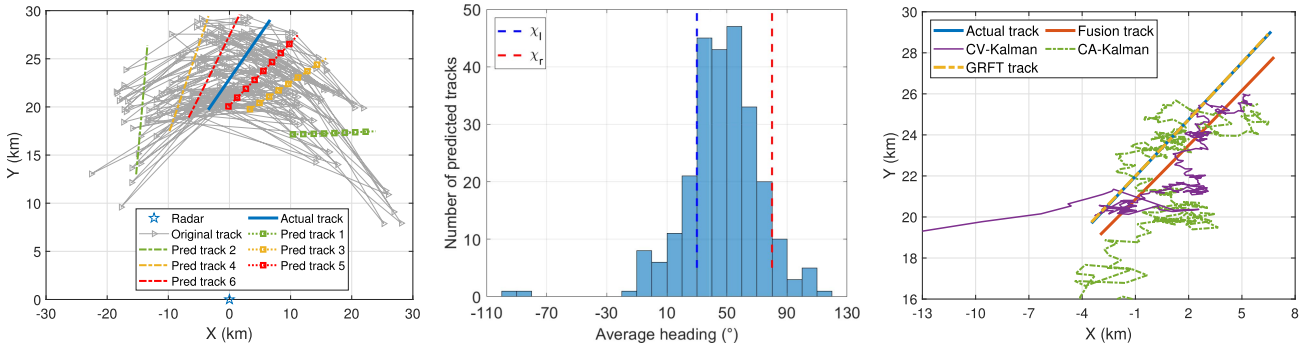

Fig. 8. Processing results of a simulated rectilinear motion. (a) Original track and six predicted tracks. (b) Histogram of the average headings of all predicted tracks. (c) GRFT track, fusion track and results of CV-Kalman filter and CA-Kalman filter.

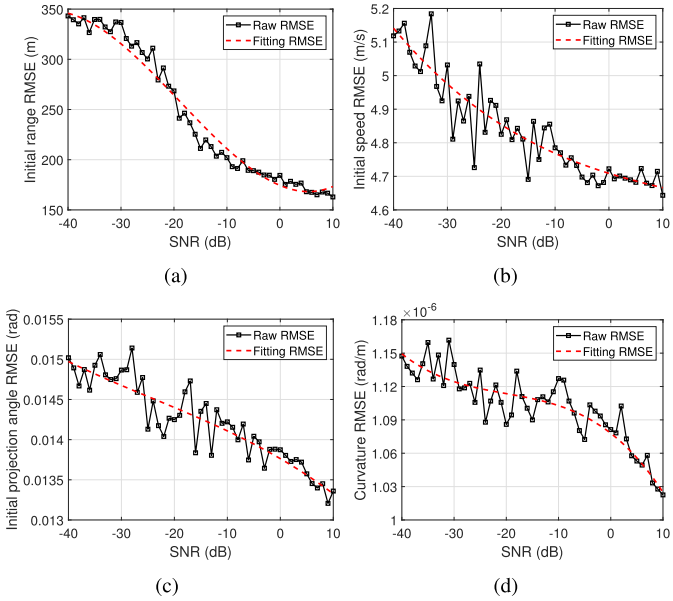

Fig. 9. RMSEs of GRFT parameter estimation. (a) Initial range. (b) Initial speed. (c) Initial projection angle. (d) Curvature.

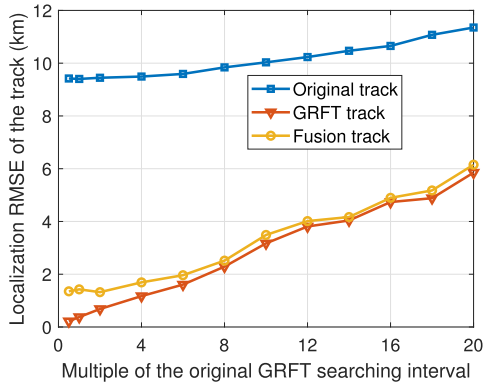

Fig. 10. Target localization RMSEs under different GRFT searching intervals.

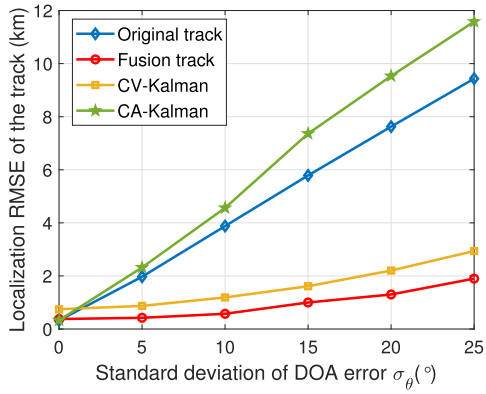

Fig. 11. Target localization RMSEs under different DOA errors.

experiment, the HF radar was about 20 km away from a civilian airport and the main observation targets were civil aircrafts.

Fig. 13 shows the transmitting and receiving antennas of the compact HF radar used in the experiment. The transmitting antenna is a monopole antenna and the receiving antenna is a CLM antenna. They are 5.8 m apart. The radar parameters are shown in Table I. The ground truth data of target tracking are from an automatic dependent surveillance-broadcast (ADS-B) system located adjacent to the radar, which can provide real-time information about aircrafts' position.

B. Field Experiment Result

Fig. 14(a) and 14(b), respectively, shows the RT map and the RD map measured by the monopole receiving antenna element within a CPI when target 2 passes through the radar coverage area. Obviously RM and DFM are present. In addition to the target echo, there are also radio frequency interference and zero frequency interference in the spectra.

As mentioned in Section III, the proposed method is based on a 2-D motion model on the horizontal plane, because the compact HF radar cannot measure the target altitude, and its tracking objects are generally ships or low-flying aircrafts at altitudes ($<$1km) much less than their ranges. However, the observation targets of the field experiment in this article are civil aircrafts at altitudes (6$\sim$12.6 km) comparable to their ranges. The range values in the RT spectrum are in fact slant ranges in 3-D space, which cannot be approximated as horizontal ranges if the target altitudes are high. Therefore, (9) needs to be modified

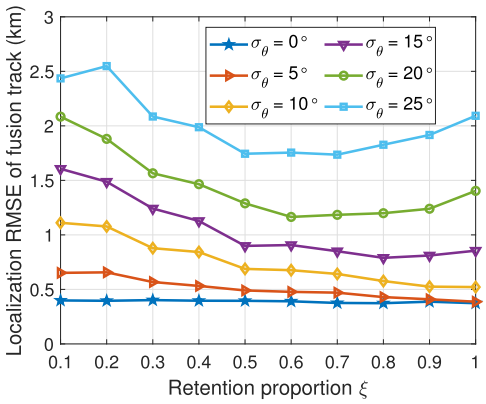

Fig. 12. Fusion track RMSEs under different retention proportions.

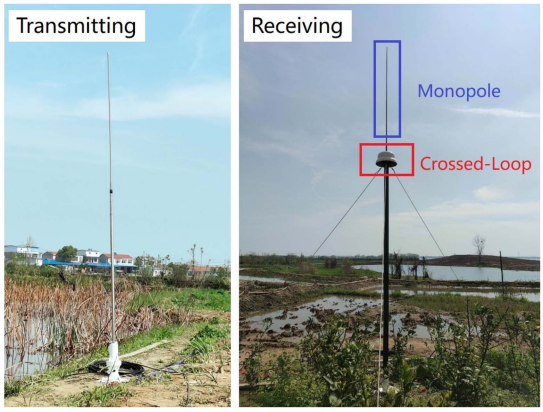

Fig. 13. Transmitting and receiving antennas of compact HF radar.

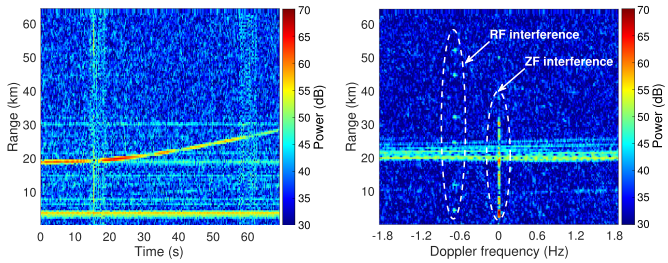

Fig. 14. Echo spectra of target 2 measured by the monopole receiving antenna within a CPI. (a) RT map. (b) RD map.

as follows:

$$r(t) = \left\{ \left[r_0 + \int_0^t v(\tau)\cos\phi(\tau)\mathrm{d}\tau \right]^2 + \left[\int_0^t v(\tau)\sin\phi(\tau)\mathrm{d}\tau \right]^2 + h^2(t) \right\}^{\frac{1}{2}} \tag{29}$$

where $r(t)$ refers to the slant range in 3-D space, and $h(t)$ is the target altitude, which is provided by the ADS-B system in this article.

Using the GRFT algorithm, the target motion parameter estimates $\hat{r}_0$, $\hat{v}_0$, $\hat{\phi}_0$, $\hat{\kappa}$ are calculated from the RT spectrum of the monopole receiving element. Then, based on (6), (7), (8), and (29), the slant range $\hat{r}_m$ at moment $t_m (m = 0, 1, \ldots, M-1)$ is calculated. After that, $\hat{r}_m$ is converted to the horizontal range $\hat{r}_m^{\mathrm{hor}}$ according to the following equation:

$$\hat{r}_m^{\mathrm{hor}} = \sqrt{\hat{r}_m^2 - h_m^2} \tag{30}$$

where h_m denotes the target altitude at moment t_m provided by the ADS-B system. Note that the target ranges in the descriptions later in Section V-B all refer to horizontal ranges.

Using the MUSIC algorithm, the DOAs are estimated from the RT spectra of the three receiving elements integrated into the CLM antenna. The range and DOA estimates are then used to calculate the original track, which is shown in Fig. 15(a). The actual track acquired by the ADS-B system is also displayed, reflecting that the target is making a curved motion. Compared with the actual track, the RMSE of the original track is 4.78 km.

The GRFT track which does not include DOA estimation errors nearly coincides with the actual track and has a much lower RMSE of 0.64 km, which indicates that the original track errors mainly come from DOA estimation errors rather than GRFT estimation errors.

The DOA estimation errors can be calculated using the data provided by the ADS-B system. The histogram of DOA estimation errors is shown in Fig. 15(b), which basically conforms to a zero-mean Gaussian distribution. The mean value is -3.82°, which is indicated by a red dashed line in Fig. 15(b). The RMSE is calculated to be 10.45°.

Fig. 15(c) shows the histogram of average headings of all predicted tracks. Following a retention proportion of $\xi = 0.8$, the lower and upper bounds of predicted track screening are respectively 45° and 70°.

Fig. 15(a) also demonstrates the fusion track and the tracks generated by the CV-Kalman filter and CA-Kalman filter, which have RMSEs of 1.71, 3.68, and 3.94 km, respectively. The fusion track has the smallest RMSE and is most similar to the actual track in morphology, which reflects the good performance of the proposed method.

Fig. 16 shows the tracking results of other six targets and their corresponding DOA estimation errors. For each target, the GRFT track is not shown because it almost overlaps with the actual track and is not the final tracking result of the proposed method. For all these six targets, the tracking results of the proposed method, i.e., the fusion tracks, are the closest to the actual tracks when compared to those of the CV-Kalman filter and CA-Kalman filter. In particular, it should be noted that the fusion track of target 3 in Fig. 16(c) is a splicing of the tracking results of two consecutive CPIs, and its consistency with the actual track reflects the potential of the proposed method for longer time target tracking.

Fig. 17 shows the RMSEs of the tracking results and DOA estimates for the above-mentioned seven targets. The seven targets are listed in order of DOA RMSE from smallest to largest. The RMSEs of the original track and the tracking results of CV-Kalman filter and CA-Kalman filter generally increase with

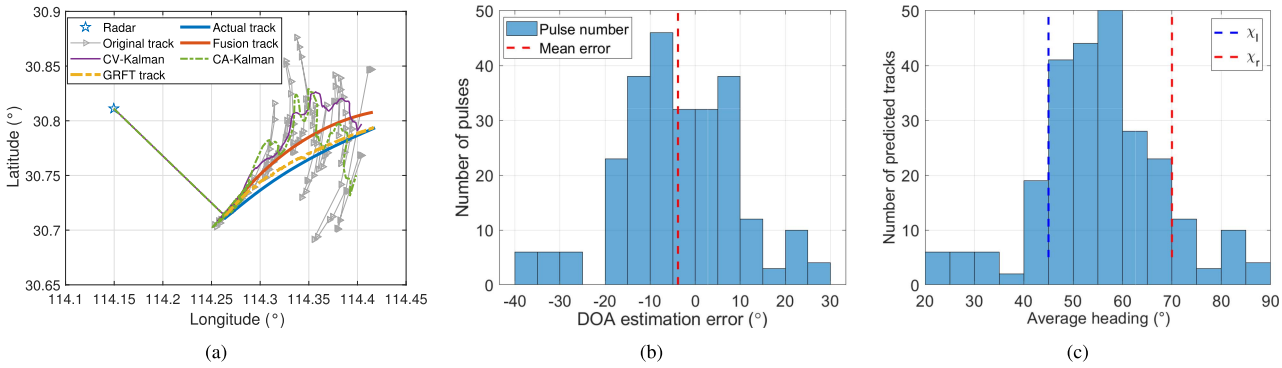

Fig. 15. Tracking results of target 2. (a) Original track, GRFT track, fusion track and results of CV-Kalman filter and CA-Kalman filter. (b) Histogram of the DOA estimation errors. (c) Histogram of the average headings of all predicted tracks.

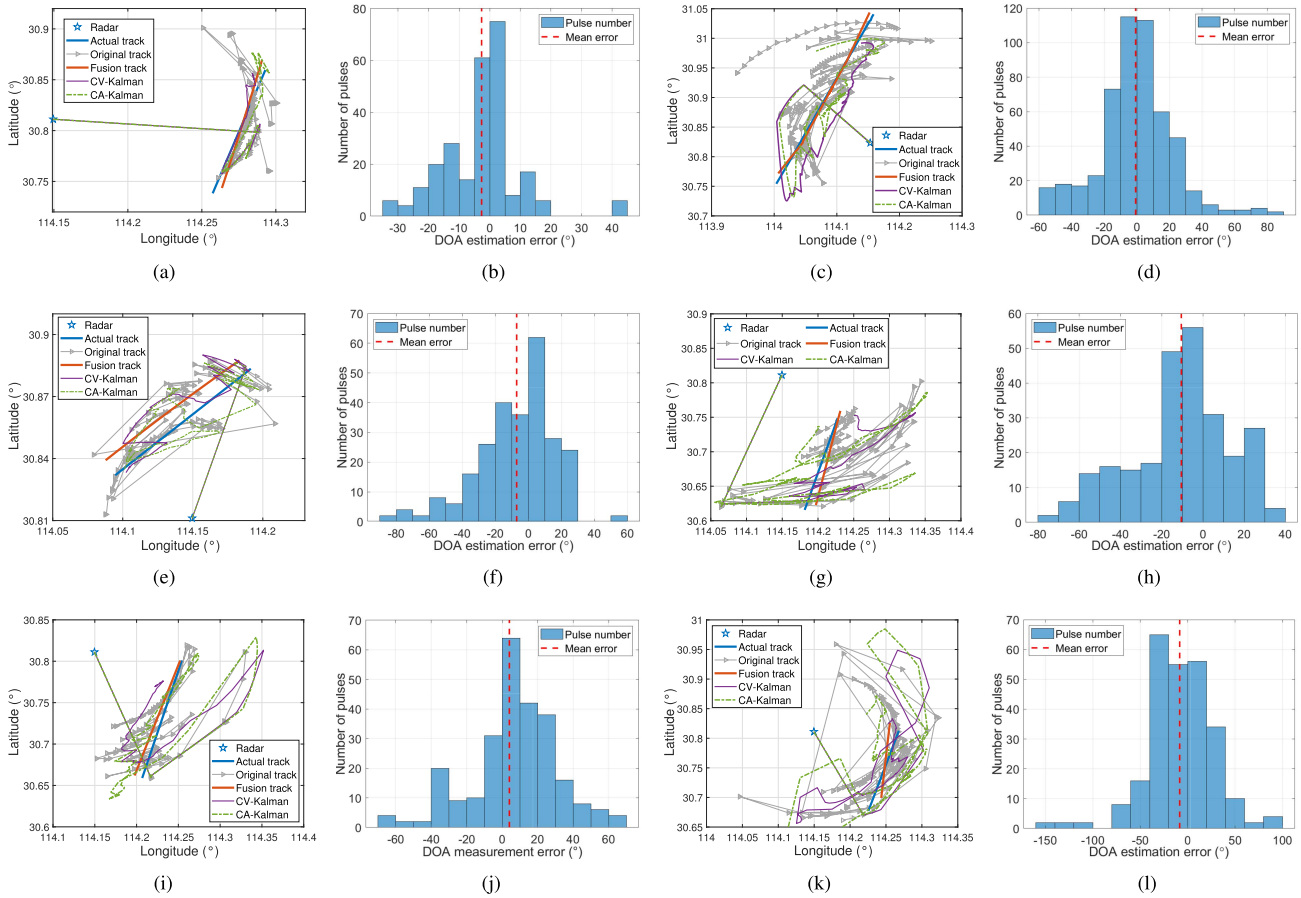

Fig. 16. Target tracking results and DOA estimation errors. (a) Tracking results of target 1. (b) Histogram of the DOA estimation errors of target 1. (c) Tracking results of target 3. (d) Histogram of the DOA estimation errors of target 3. (e) Tracking results of target 4. (f) Histogram of the DOA estimation errors of target 4. (g) Tracking results of target 5. (h) Histogram of the DOA estimation errors of target 5. (i) Tracking results of target 6. (j) Histogram of the DOA estimation errors of target 6. (k) Tracking results of target 7. (l) Histogram of the DOA estimation errors of target 7.

the increase of DOA RMSE, except for target 4 and target 6. The reason is that the ranges of target 4 and 6 are smaller than the ranges of target 3 and 5 in front of them, respectively, and if the DOA error is constant, the closer the target range is, the smaller the target localization error is. To confirm this, the ranges of the six targets are plotted with a blue line.

In contrast, the fusion tracks are much less affected by DOA RMSEs. The minimum value of fusion track RMSEs of the seven targets is 0.64 km (target 6) and the maximum value is 2.08 km (target 7). Even for DOA RMSEs above 25°, the proposed method achieves good tracking results.

C. Discussion

1) CLM Pattern Distortion: The effectiveness of the proposed method is based on the property that the mean value

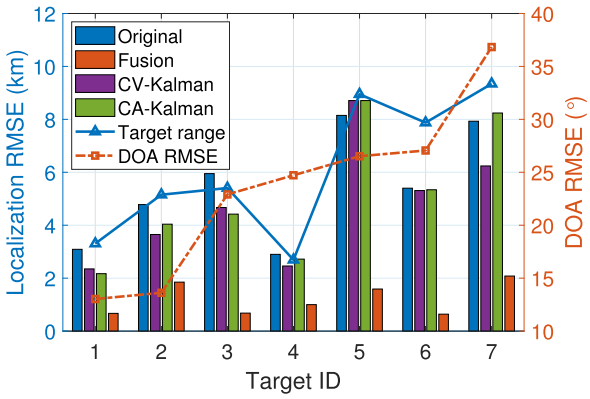

Fig. 17. RMSEs of tracking results and DOA estimates for seven targets.

of the DOA estimation error is zero. However, in practice, the DOA estimation error does not strictly conform to this, as can be seen in Figs. 15(b), 16(b), (d), (f), (h), (j), and (i). The reason is that the CLM antenna patterns are distorted by the surrounding electromagnetic environment, but the ideal CLM antenna patterns without distortion are used by the MUSIC algorithm for DOA estimation [47].

From Figs. 15 and 16, it can be seen that the proposed method still achieves good performance although the mean DOA error deviates from zero. If the ideal patterns used in DOA estimation are replaced by the actual patterns obtained from field measurement, the mean value of DOA estimation error will approach zero [21], and it can be predicted that the proposed method will achieve better tracking performance, but of course, more experiments are needed to verify this.

2) Sea Clutter: Compact HF radars monitor mainly sea surface targets, including ships and low-altitude aircrafts. However, in order to facilitate testing of the proposed method, the field experiment in this article is conducted inland. Compared with experiment at the seashore, a big difference is the lack of interference from sea clutter.

Sea clutter is distributed over multiple range bins at the same time, thus inevitably deteriorates target tracking when its power is strong. However, the Doppler frequency of sea clutter is concentrated around the Bragg frequency [48], which is significantly different from the high-speed targets of concern in this article. Taking advantage of this, it is promising to suppress the sea clutter prior to target tracking, so as to weaken its effect. This needs to be verified in future experiments.

3) Computational Cost: The computational cost of the proposed method mainly comes from two phases, one is the original track estimation phase and the other is the track optimization phase. The former includes the use of GRFT algorithm, MUSIC algorithm and the synthesis of original track, and the latter consists of track prediction, screening, and fusion.

Both the CV-Kalman filter and the CA-Kalman filter, which are used in this article for comparison with the proposed method, are applied on the basis of the original track. Therefore, their computational complexity should also include the complexity from the original track estimation, and thus differ from that of the proposed method only in the track optimization phase.

In the original track estimation phase, the computational complexity of the GRFT algorithm [17] is $O(N_r N_v N_\phi N_\kappa M)$, where N_r, N_v, N_ϕ, and N_κ are the number of searching initial ranges, searching initial speeds, searching initial projection angles and searching curvature values, respectively. The computational complexity of the MUSIC algorithm [49] is $O(N_a^2 M + N_a^3 M + N_a^2 N_d M)$, where N_d is the number of searching DOA values, and the three addends in parentheses correspond to the computational complexity of covariance matrix calculation, eigenvalue decomposition, and MUSIC spectrum estimation, respectively. The computational complexity of original track synthesis is $O(M)$.

In the track optimization phase, the computation complexity of the proposed method is $O(M^2)$. The computational complexity of Kalman filtering algorithm is mainly related to the number of state variables N_e and the number of measurement variables N_m [50], [51]. Therefore, in the track optimization phase, the computational complexity of the CV-Kalman filter is $O((M-1)(N_e^3 + N_e^2 N_m + N_e N_m^2 + N_m^3))$, where $N_e = 4$ and $N_m = 2$, and that of the CA-Kalman filter is $O((M-2)(N_e^3 + N_e^2 N_m + N_e N_m^2 + N_m^3))$, where $N_e = 6$ and $N_m = 2$. It can be seen that if M is large, the computational complexity of the proposed method will exceed that of the other two methods, but under the value of $M = 256$ set in this article, the computational complexity of the three methods is not much different.

The GRFT algorithm, which is implemented through an exhaustive search approach in multiple dimensions, accounts for a large portion of the computational cost. However, GRFT in the proposed method can be replaced by other coherent integration algorithms with lower computational complexity, such as Radon-fractional Fourier transform [52], Radon Lv's distribution [53], and adjacent cross-correlation function [54]. These algorithms reduce computational costs by sacrificing a certain amount of coherent integration gain. Furthermore, incoherent integration algorithms with lower computational costs can also be applied here to enhance the real-time performance of the proposed method, such as generalized Radon transform [55] and Hough transform [56], which yet have reduced detection capabilities for weak targets.

4) Multitarget Tracking: Both simulations and field experiments in this article investigate only the tracking of a single target. When there are multiple targets in the RT spectrum, a long time coherent accumulation algorithm (not necessarily GRFT, other long time accumulation algorithms also work) combined with the CLEAN algorithm can be used to detect these targets and estimate their motion parameters, which has been shown to be effective [57], [58]. Then, for each target, the original track can be estimated and optimized using the method proposed in this article. For the case that there are numerous and overlapping targets in the RT spectrum, the performance of the proposed method still needs to be further verified.

VI. Conclusion

This article presents a high-speed target tracking method for compact HF radar. High-speed targets in this article refer to those that cause significant RM and DFM. RM and DFM not only

increase the difficulty of target detection and motion parameter estimation, but also reduce the accuracy of DOA estimation and thus deteriorate the tracking performance. In this article, GRFT algorithm is used to detect the target and estimate its motion parameters. In addition, using the zero mean distribution of DOA estimation error, this article realizes DOA error cancellation by averaging multiple predicted tracks corresponding to different DOA estimates, thereby reducing the influence of DOA error on tracking accuracy.

The proposed method mainly includes four steps. First, the motion parameters of the target are estimated using the GRFT algorithm, the DOA of the target is estimated using the MUSIC algorithm, and the original track is calculated based on the estimates of range and DOA. Then, multiple base points are selected from the original track, and for each base point, a predicted track is calculated, thus multiple predicted tracks are obtained. The predicted tracks are then screened based on their average headings. Finally, the screened predicted tracks are fused to generate the final track.

Numerical simulation and field experiment demonstrate the good performance of the proposed method. Compared with the commonly used tracking methods CV-Kalman filter and CA-Kalman filter, the proposed method significantly reduces the error of the original track, especially when the DOA error is large, the superiority of the proposed method is more prominent.

As mentioned in Section III-B, the proposed method requires a constant trend in target's DOA over a CPI. This requirement is not satisfied in some cases, e.g., when the target makes a circular motion with large curvature. This problem may be solved by reducing the CPI and jointly processing the tracking results of multiple CPIs, which needs more in-depth research in the future.

In this article, the field experiment site is near an inland civil airport and the tracking targets are civil aircrafts, but the compact HF radar is designed to track targets sailing on the sea surface or flying at low altitude over the sea. Therefore, field experiments at the seashore need to be carried out in the future to test the performance of the proposed method.

REFERENCES

[1] J. M. Headrick and M. I. Skolnik, "Over-the-horizon radar in the HF band," *Proc. IEEE*, vol. 62, no. 6, pp. 664–673, Jun. 1974.

[2] S. Saviano, A. Kalampokis, E. Zambianchi, and M. Uttieri, "A year-long assessment of wave measurements retrieved from an HF radar network in the Gulf of Naples (Tyrrhenian Sea, Western Mediterranean Sea)," *J. Oper. Oceanogr.*, vol. 12, no. 1, pp. 1–15, 2019.

[3] C. Wang et al., "Validation and intercomparison of sea state parameter estimation with multisensors for OSMAR-S high-frequency radar," *IEEE Trans. Instrum. Meas.*, vol. 69, no. 10, pp. 7552–7565, Oct. 2020.

[4] Z. Tian, Y. Tian, B. Wen, and J. Zhao, "Wave-height map extraction from compact HF surface-wave radar network," *IEEE Geosci. Remote Sens. Lett.*, vol. 18, no. 1, pp. 77–81, Jan. 2021.

[5] Y. Zeng, H. Zhou, Z. Tian, and B. Wen, "Mapping wind by the first-order Bragg scattering of broad-beam high-frequency radar," *Acta Oceanol. Sinica*, vol. 40, no. 3, pp. 153–166, 2021.

[6] S. Park, C. J. Cho, B. Ku, S. Lee, and H. Ko, "Compact HF surface wave radar data generating simulator for ship detection and tracking," *IEEE Geosci. Remote Sens. Lett.*, vol. 14, no. 6, pp. 969–973, Jun. 2017.

[7] W. Sun et al., "A vessel azimuth and course joint re-estimation method for compact HFSWR," *IEEE Trans. Geosci. Remote Sens.*, vol. 58, no. 2, pp. 1041–1051, Feb. 2020.

[8] Y. Tian, S. Ma, H. Zhou, and J. Zhao, "Robust track association for ship localization with multiple compact HF radars," *IEEE Trans. Geosci. Remote Sens.*, vol. 61, 2023, Art. no. 5109711.

[9] K. E. Laws, J. F. Vesecky, M. N. Lovellette, and J. D. Paduan, "Ship tracking by HF radar in coastal waters," in *Proc. MTS/IEEE OCEANS Conf.*, Monterey, CA, USA, 2016, pp. 1–8.

[10] G. Vivone, P. Braca, and J. Horstmann, "Knowledge-based multitarget ship tracking for HF surface wave radar systems," *IEEE Trans. Geosci. Remote Sens.*, vol. 53, no. 7, pp. 3931–3949, Jul. 2015.

[11] P. P. Gandhi and S. A. Kassam, "Analysis of CFAR processors in non-homogeneous background," *IEEE Trans. Aerosp. Electron. Syst.*, vol. 24, no. 4, pp. 427–445, Jul. 1988.

[12] D. Kundu, "Modified MUSIC algorithm for estimating DOA of signals," *Signal process.*, vol. 48, no. 1, pp. 85–90, 1996.

[13] D. E. Barrick and B. J. Lipa, "Evolution of bearing determination in HF current mapping radars," *Oceanography*, vol. 10, no. 2, pp. 72–75, 1997.

[14] Z. Li, B. Wen, and Y. Tian, "Design and implementation of a dual-frequency compact antenna system for HF radar," *IEEE Antennas Wireless Propag. Lett.*, vol. 16, pp. 1887–1890, 2017.

[15] Y. Ji et al., "Ship monitoring with bistatic compact HFSWR of small aperture," *IEEE J. Sel. Topics Appl. Earth Observ. Remote Sens.*, vol. 15, pp. 1139–1149, 2022.

[16] A. Dzvonkovskaya and H. Rohling, "Fast-moving target observation using high-frequency surface wave radar," in *Proc. Int. Radar Conf.*, Lille, France, 2014, pp. 1–4.

[17] J. Xu, J. Yu, Y.-N. Peng, and X.-G. Xia, "Radon-Fourier transform for radar target detection (I): Generalized Doppler filter bank," *IEEE Trans. Aerosp. Electron. Syst.*, vol. 47, no. 2, pp. 1186–1202, Apr. 2011.

[18] J. Xu, J. Yu, Y.-N. Peng, and X.-G. Xia, "Radon-Fourier transform for radar target detection (II): Blind speed sidelobe suppression," *IEEE Trans. Aerosp. Electron. Syst.*, vol. 47, no. 4, pp. 2473–2489, Oct. 2011.

[19] J. Yu, J. Xu, Y.-N. Peng, and X.-G. Xia, "Radon-Fourier transform for radar target detection (III): Optimality and fast implementations," *IEEE Trans. Aerosp. Electron. Syst.*, vol. 48, no. 2, pp. 991–1004, Apr. 2012.

[20] A. Belouchrani and M. G. Amin, "Time-frequency MUSIC," *IEEE Signal Process. Lett.*, vol. 6, no. 5, pp. 109–110, May 1999.

[21] Y. Tian, B. Wen, J. Tan, and Z. Li, "Study on pattern distortion and DOA estimation performance of crossed-loop/monopole antenna in HF radar," *IEEE Trans. Antennas Propag.*, vol. 65, no. 11, pp. 6095–6106, Nov. 2017.

[22] J. Zhao, Y. Tian, B. Wen, and Z. Tian, "Coherent DOA estimation in sea surface observation with direction-finding HF radar," *IEEE Trans. Geosci. Remote Sens.*, vol. 59, no. 8, pp. 6651–6661, Aug. 2021.

[23] Y. Lai, H. Zhou, Y. Zeng, and B. Wen, "Ocean surface current observation with a dual monopole-cross-loop antenna array," *Int. J. Antennas Propag.*, vol. 2017, 2017, Art. no. 2754831.

[24] G. Welch et al., *An Introduction to the Kalman Filter*. Chapel Hill, NC, USA: Univ. of North Carolina Press, 1995.

[25] S.-T. Park and J. G. Lee, "Improved Kalman filter design for three-dimensional radar tracking," *IEEE Trans. Aerosp. Electron. Syst.*, vol. 37, no. 2, pp. 727–739, Apr. 2001.

[26] P. M. Djuric et al., "Particle filtering," *IEEE Signal Process. Mag.*, vol. 20, no. 5, pp. 19–38, Sep. 2003.

[27] P. R. Kalata, "The tracking index: A generalized parameter for α-β and α-β-γ target trackers," *IEEE Trans. Aerosp. Electron. Syst.*, vol. AES- 20, no. 2, pp. 174–182, Mar. 1984.

[28] R. Su, J. Tang, J. Yuan, and Y. Bi, "Nearest neighbor data association algorithm based on robust Kalman filtering," in *Proc. 2nd Int. Symp. Comput. Eng. Intell. Commun. (ISCEIC)*, Nanjing, China, 2021, pp. 177–181.

[29] S. S. Blackman, "Multiple hypothesis tracking for multiple target tracking," *IEEE Aerosp. Electron. Syst. Mag.*, vol. 19, no. 1, pp. 5–18, Jan. 2004.

[30] T. Fortmann, Y. Bar-Shalom, and M. Scheffe, "Sonar tracking of multiple targets using joint probabilistic data association," *IEEE J. Ocean. Eng.*, vol. 8, no. 3, pp. 173–184, Jul. 1983.

[31] W. Kazimierski and A. Stateczny, "Optimization of multiple model neural tracking filter for marine targets," in *Proc. 13th Int. Radar Symp.*, Warsaw, Poland, May 2012, pp. 543–548.

[32] S. Mahfouz, F. Mourad-Chehade, P. Honeine, J. Farah, and H. Snoussi, "Target tracking using machine learning and Kalman filter in wireless sensor networks," *IEEE Sensors J.*, vol. 14, no. 10, pp. 3715–3725, Oct. 2014.

[33] S. Maresca, P. Braca, J. Horstmann, and R. Grasso, "Maritime surveillance using multiple high-frequency surface-wave radars," *IEEE Trans. Geosci. Remote Sens.*, vol. 52, no. 8, pp. 5056–5071, Aug. 2014.

[34] D. Nikolic et al., "Maritime over the horizon sensor integration: HFSWR data fusion algorithm," *Remote Sens.*, vol. 11, no. 7, 2019, Art. no. 852.

[35] J. Xu, X.-G. Xia, S.-B. Peng, J. Yu, Y.-N. Peng, and L.-C. Qian, "Radar maneuvering target motion estimation based on generalized Radon-Fourier transform," *IEEE Trans. Signal Process.*, vol. 60, no. 12, pp. 6190–6201, Dec. 2012.
[36] P. Stoica and A. Nehorai, "MUSIC, maximum likelihood, and Cramer-Rao bound," *IEEE Trans. Acoust., Speech, Signal Process.*, vol. 37, no. 5, pp. 720–741, May 1989.
[37] A. De Maio, L. Pallotta, J. Li, and P. Stoica, "Loading factor estimation under affine constraints on the covariance eigenvalues with application to radar target detection," *IEEE Trans. Aerosp. Electron. Syst.*, vol. 55, no. 3, pp. 1269–1283, Jun. 2019.
[38] M. Steiner and K. Gerlach, "Fast converging adaptive processor or a structured covariance matrix," *IEEE Trans. Aerosp. Electron. Syst.*, vol. 36, no. 4, pp. 1115–1126, Oct. 2000.
[39] A. Aubry, A. De Maio, and L. Pallotta, "A geometric approach to covariance matrix estimation and its applications to radar problems," *IEEE Trans. Signal Process.*, vol. 66, no. 4, pp. 907–922, Feb. 2018.
[40] X. Chen, X. Yu, Y. Huang, and J. Guan, "Adaptive clutter suppression and detection algorithm for radar maneuvering target with high-order motions via sparse fractional ambiguity function," *IEEE J. Sel. Topics Appl. Earth Obs. Remote Sens.*, vol. 13, pp. 1515–1526, 2020.
[41] W. Sun, W. Huang, Y. Ji, Y. Dai, P. Ren, and P. Zhou, "Vessel tracking with small-aperture compact high-frequency surface wave radar," in *Proc. MTS/IEEE Oceans*, Marseille, France, 2019, pp. 1–4.
[42] W. Sun, M. Ji, W. Huang, Y. Ji, and Y. Dai, "Vessel tracking using bistatic compact HFSWR," *Remote Sens.*, vol. 12, no. 8, 2020, Art. no. 1266.
[43] M. I. Skolnik, *Introduction to Radar Systems*. New York, NY, USA: McGraw-Hill Educ., 2002.
[44] T. Jian, "Design and implementation of high-frequency ground wave radar waveform based on multi-sweep frequency," Ph.D. dissertation, Wuhan Univ., Wuhan, China, 2016.
[45] C. Trueman, S. Kubina, S. Mishra, and C. Larose, "RCS of four fuselage-like scatterers at HF frequencies," *IEEE Trans. Antennas Propag.*, vol. 40, no. 2, pp. 236–240, Feb. 1992.
[46] C. Trueman, S. Kubina, S. Mishra, and C. Larose, "Radar cross-section of a generic aircraft at HF frequencies," *Can. J. Elect. Comput. Eng.*, vol. 18, no. 2, pp. 59–64, 1993.
[47] Y. Lai, H. Zhou, Y. Zeng, and B. Wen, "Relationship between DOA estimation error and antenna pattern distortion in direction-finding high-frequency radar," *IEEE Geosci. Remote Sens. Lett.*, vol. 16, no. 8, pp. 1235–1239, Aug. 2019.
[48] J. Zhao, B. Wen, Y. Tian, Z. Tian, and S. Wang, "Sea clutter suppression for shipborne HF radar using cross-loop/monopole array," *IEEE Geosci. Remote Sens. Lett.*, vol. 16, no. 6, pp. 879–883, Jun. 2019.
[49] R. Schmidt, "Multiple emitter location and signal parameter estimation," *IEEE Trans. Antennas Propag.*, vol. 34, no. 3, pp. 276–280, Mar. 1986.
[50] R. S. Baheti, "Efficient approximation of Kalman filter for target tracking," *IEEE Trans. Aerosp. Electron. Syst.*, vol. AES-22, no. 1, pp. 8–14, Jan. 1986.
[51] C.-S. Hsieh and F.-C. Chen, "Optimal solution of the two-stage Kalman estimator," *IEEE Trans. Automat. Control*, vol. 44, no. 1, pp. 194–199, Jan. 1999.
[52] X. Chen, J. Guan, N. Liu, and Y. He, "Maneuvering target detection via Radon-fractional Fourier transform-based long-time coherent integration," *IEEE Trans. Signal Process.*, vol. 62, no. 4, pp. 939–953, Feb. 2014.
[53] X. Chen, J. Guan, X. Li, and Y. He, "Effective coherent integration method for marine target with micromotion via phase differentiation and Radon-Lv's distribution," *IET Radar, Sonar Navigation*, vol. 9, no. 9, pp. 1284–1295, 2015.
[54] X. Li, G. Cui, W. Yi, and L. Kong, "A fast maneuvering target motion parameters estimation algorithm based on ACCF," *IEEE Signal Process. Lett.*, vol. 22, no. 3, pp. 270–274, Mar. 2015.
[55] G. Beylkin, "The inversion problem and applications of the generalized Radon transform," *Commun. Pure Appl. Math.*, vol. 37, no. 5, pp. 579–599, 1984.
[56] B. Carlson, E. Evans, and S. Wilson, "Search radar detection and track with the Hough transform. I. System concept," *IEEE Trans. Aerosp. Electron. Syst.*, vol. 30, no. 1, pp. 102–108, Jan. 1994.
[57] J. Tsao and B. D. Steinberg, "Reduction of sidelobe and speckle artifacts in microwave imaging: The CLEAN technique," *IEEE Trans. Antennas Propag.*, vol. 36, no. 4, pp. 543–556, Apr. 1988.
[58] J. Misiurewicz, K. S. Kulpa, Z. Czekala, and T. A. Filipek, "Radar detection of helicopters with application of CLEAN method," *IEEE Trans. Aerosp. Electron. Syst.*, vol. 48, no. 4, pp. 3525–3537, Oct. 2012.

Gan Liu was born in Hubei, China, in 1995. He received the B.Eng. degree in electronic information engineering from Hubei University of Arts and Sciences, Xiangyang, China, in 2017, and the M.S. degree in circuits and system from Kunming University of Science and Technology, Kunming, China, in 2020. He is currently working toward the Ph.D. degree in electronic information with Wuhan University, Wuhan, China.

His research interests include target detection and tracking using high-frequency radar.

Yingwei Tian (Member, IEEE) was born in Qianjiang, Hubei, China, in 1989. He received the B.Eng. degree in communication engineering and the Ph.D. degree in communication and information systems from Wuhan University, Wuhan, China, in 2010 and 2015, respectively.

From 2015 to 2018, he was a Postdoctoral Fellow in geophysics with Wuhan University, where he is currently an Associate Processor. From 2018 to 2019, he was a Visiting Scholar with Memorial University, St. John's, NL, Canada. His research interests include the hardware design and signal processing of HF and UHF radar systems, and their application to the ocean surface remote sensing.

Jing Yang (Member, IEEE) was born in Xiangyang, Hubei, China, in 1983. She received the B.E. degree in electronic information science and technology and the Ph.D. degree in communication and information systems from Wuhan University, Wuhan, China, in 2005 and 2010, respectively.

Since 2011, she has been with the School of Electronic Information, Wuhan University. Her research interests include ocean surface remote sensing and signal processing.

Shengbo Ma born in Shandong, China, in 1999. He received the bachelor's degree in engineering from South Central University for Nationalities in Wuhan, China, in 2017 and the Master's degree degree in engineering from Wuhan University in 2024.

His research focuses on detecting vessel targets and optimizing their tracks using high-frequency ground wave radar.

Biyang Wen was born in Hubei, China, in 1963. He received the B.Eng. degree in precision instrument from Shanghai Jiao Tong University, Shanghai, China, in 1983, the M.S. degree in radio electronics and Ph.D. degree in space physics from Wuhan University, Wuhan, China, in 1990 and 1997, respectively.

Since 1990, he has been with the School of Electronic Information, Wuhan University, where he is currently a Professor. His research interests include radio wave propagation and remote sensing of the ocean surface via high-frequency ground wave radar and UHF radar.